MATERIALS SCIENCE

Defects and plasticity in ultrastrong supercrystalline nanocomposites

D. Giuntini[1]*†, S. Zhao[2], T. Krekeler[3], M. Li[4], M. Blankenburg[4], B. Bor[1], G. Schaan[3], B. Domènech[1], M. Müller[4], I. Scheider[4], M. Ritter[3], G. A. Schneider[1]

Supercrystalline nanocomposites are nanoarchitected materials with a growing range of applications but unexplored in their structural behavior. They typically consist of organically functionalized inorganic nanoparticles arranged into periodic structures analogous to crystalline lattices, including superlattice imperfections induced by processing or mechanical loading. Although featuring a variety of promising functional properties, their lack of mechanical robustness and unknown deformation mechanisms hamper their implementation into devices. We show that supercrystalline materials react to indentation with the same deformation patterns encountered in single crystals. Supercrystals accommodate plastic deformation in the form of pile-ups, dislocations, and slip bands. These phenomena occur, at least partially, also after cross-linking of the organic ligands, which leads to a multifold strengthening of the nanocomposites. The classic shear theories of crystalline materials are found to describe well the behavior of supercrystalline nanocomposites, which result to feature an elastoplastic behavior, accompanied by compaction.

INTRODUCTION

Nanostructured composite materials are a fast-growing field of materials science and engineering, thanks to their very broad range of applications and the development of processing techniques optimized for the nanoscale (*1*). Supercrystalline materials are a subcategory of nanostructured composites, characterized by a special architecture: The constituent inorganic nanobuilding blocks, typically surface functionalized with an organic ligand, are arranged into periodic structures reminiscent of crystalline lattices, often called superlattices. Similar or analogous materials can also be found in the literature under the name of supracrystals or under the broader category of mesocrystals (*2*–*4*). They have initially been developed in the form of thin films or micrometer-sized single supercrystals (*5*), but they are being upscaled into larger bulk poly-supercrystalline materials (*2*, *6*–*9*). They find applications in a wide variety of fields, some established and some still in their infancy, from energy storage to optoelectronics and from catalysts and sensors to biomedical products (*3*, *5*, *10*–*14*). An important limitation for the embedding of supercrystalline nanocomposites into devices is often their lack of mechanical robustness (*1*). The mechanical properties of supercrystals—typically assessed via nanoindentation or atomic force microscopy (AFM)—are comparable to the ones of hard polymers (*15*–*19*).

Some recent studies of this same group have made a step forward in this direction, showing that by cross-linking, the organic chains at the interfaces between the nanoparticles that form the superlattice, a marked improvement in the material's mechanical response, are induced (*2*, *7*–*9*). The weak interactions that typically hold together the supercrystals' building blocks (van der Waals–dominated) become overridden by a network of covalent bonds, resulting in a shift from soft matter to strong inorganic-organic nanocomposites. The nanocomposites become therefore much stronger, stiffer, and harder (bending strength, elastic modulus, and hardness of up to 630 MPa, 60 GPa, and 4.7 GPa, respectively) (*2*, *7*). A substantial increase in the fracture toughness is also achieved (~0.5 $MPa{\cdot}m^{1/2}$, one order of magnitude higher than previously reported values and theoretical estimations), accompanied by a reduction of the cracking and chipping phenomena resulting from indentation tests (*7*). What deformation behavior is associated with these enhanced mechanical properties, as well as whether significant alterations are introduced with the cross-linking of the organic phase, is what this paper aims at unveiling, through correlations between mechanical testing and nanostructural features.

Superlattices can show nanostructure defects analogous to the ones normally found in atomic crystalline lattices, and these are expected to play an important role in the supercrystals' mechanical response (*1*, *20*). A general analogy between atoms in crystals and nanoparticles in supercrystals has been proposed (*21*). Typically, zero-dimensional (0D) and 1D defects are observed in the form of vacancies and interstitials as point defects and dislocations as line defects (*22*, *23*). It is, however, important to distinguish between process-induced defects and deformation-induced defects. The formers have been explored in colloidal crystals, which are becoming a platform to study the dynamics of atomic crystals' nucleation, growth, melting, and phase transformation phenomena (*24*–*27*). Colloidal systems are also being used to follow dislocation nucleation, motion, and interactions in 2D materials for photonic applications (*28*, *29*). On the other hand, the defects and deformation patterns associated with mechanical loading have only rarely been explored and, to the best of our knowledge, never for cross-linking–strengthened nanocomposite supercrystals (*30*–*33*).

We show here that supercrystalline inorganic-organic nanocomposites feature defects and mechanical deformation mechanisms analogous to the ones of atomic crystals. The distinguishing features of plasticity are detected in materials both with and without cross-linking of the organic phase. Nanoindentation does not only lead to dislocation nucleation but also to the formation of pile-ups and slip bands

[1]Institute of Advanced Ceramics, Hamburg University of Technology, Hamburg, Germany. [2]Department of Materials Science and Engineering, University of California, Berkeley, Berkeley 94720, USA. [3]Electron Microscopy Unit, Hamburg University of Technology, Hamburg, Germany. [4]Institute of Materials Research, Helmholtz-Zentrum Geesthacht, Geesthacht, Germany.
*Corresponding author. Email: diletta.giuntini@tuhh.de
†Present address: Department of Mechanical Engineering, Eindhoven University of Technology, P.O. Box 513, 5600 MB Eindhoven, Netherlands.

and is thus here described in terms of (super)crystalline plasticity and theoretical strength models. The cross-linking controls the processes that lead to these plastic deformations and limits the extension of shear deformation patterns, while a deformation mechanism additional to the ones typical of atomic crystals—material compaction—is detected.

RESULTS AND DISCUSSION

Supercrystalline nanocomposites' processing and nanostructure

The studied supercrystalline materials consist of iron oxide (magnetite, Fe_3O_4) spherical nanoparticles with a radius of 7.9 ± 1.3 nm and surface functionalized with oleic acid (see Materials and Methods for the processing routine) (*34*). A decisive processing step is the application of a moderate heat treatment, after the self-assembly of the functionalized nanoparticles into a superlattice. Heat treatment (325°C) induces the cross-linking of the organic ligands and thus the enhancement of the mechanical properties (*2*, *7*). According to small-angle x-ray scattering (SAXS) measurements (text S1 and fig. S1), the resulting supercrystals are of the face-centered cubic (FCC) type, with a lattice constant of 25.7 nm for the preheat treatment material and 24.5 nm for the heat-treated one, corresponding to an interparticle spacing (filled with organic material) of 2.4 and 1.5 nm, respectively, in the tightly packed <110> directions. These values hint at interdigitation and bending of the organic ligands, since, at full extension, the oleic acid molecules approach a length of 2 nm.

Nanoindentation was performed to measure elastic modulus and hardness and to subsequently assess the material's deformation behavior. To visualize the supercrystalline structure, defects, and deformations, we used a combination of AFM, scanning electron microscopy (SEM), and transmission electron microscopy (TEM; also operated in scanning/transmission mode, STEM) on 100-nm-thick lamellae produced via focused ion beam (FIB). All technical details on mechanical testing and nanostructure analysis are given in Materials and Methods.

The distinguishing features of these materials are (i) their bulk macroscopic form (order of cubic millimeter), thus their polysupercrystalline structure, and (ii) their remarkable combination of mechanical properties, thanks to the cross-linking of the organic phase. Successful fabrication of bulk supercrystalline nanocomposites leads to the development of a very broad set of superlattice imperfections, ranging from point defects (interstitials and vacancies) to line (dislocations), surface/interface (grain boundaries), and volume defects (pores and cracks). These imperfections can be both processing- or deformation-induced, and, in both cases, correlations with the overall mechanical response emerge.

Figure 1 shows examples of superlattice defects, detected in pristine materials (and thus originated from processing and not induced by mechanical loading). Because of the large scale of our processing routine, supercrystal nucleation is expected at multiple locations, and the subsequent contact of the various seeds is at the origin of the development of multiple types of interfaces. An additional source of imperfections is the unavoidable size scatter of the constituent nanoparticles (a size scatter of >20% often leads to "superamorphous" structures) (*8*). Figure 1A shows a supercrystalline area with uniform orientation, with a photograph of the respective bulk pellet in the inset. Figure 1B shows two neighboring supercrystalline domains with varying orientation, analogous to a high-angle grain boundary, while Fig. 1C features an example of low-angle tilt (intersupercrystalline) grain boundary. The nanoparticle planes oriented quasi-parallel to the boundary appear to belong to the {111} family, as also confirmed by the measured interplanar distance (on average, 14.1 nm, as expected, given the superlattice constant of 24.5 nm). The classic crystalline description of low-angle grain boundaries is here applied. If the tilt angle, θ, is lower than 15°, then the distance among dislocations along the boundary, D, is related to tilt angle and dislocations' Burgers vector modulus, b, as $D \sim b/\theta$. Extracting D and θ from image analysis, we find b = 15.7 nm, while the value obtained via direct measurement on the micrographs is b ~ 14.3 nm (see text S2 and fig. S2). Dislocation-like structures are found also in the form of Frank partials (or extrinsic faults; Fig. 1D), while Fig. 1E shows twins inside an otherwise uniform superlattice, leading to the following stacking sequence of (111) planes: *ABCA**CBCA**BAB**CABCABC**ACA**BCABC**ACA**BC*.

Indentation-induced defects

To evaluate loading-induced defects and deformations, we performed nanoindentation. Nanoindentation typically induces a set of lattice alterations in atomic crystals, such as pile-ups, slip bands, and specific tension-compression patterns, which are associated with crystal plasticity. It is therefore a valuable tool to assess whether supercrystals are able to deform plastically. The measured elastic (Young's) modulus and hardness revealed the expected cross-linking–induced increase: before cross-linking, E = 14.8 ± 1.1 GPa and H = 0.60 ± 0.08 GPa; after cross-linking, E = 64.1 ± 5.8 GPa and H = 4.72 ± 0.62 GPa. The presence of cross-linking also alters the features of the residual indents. Figure 2 (A to D) shows indents in non–cross-linked material, while Fig. 2 (E to H) shows the cross-linked case. In the SEM images of the Berkovich indents, one can identify the removal of a few layers of nanoparticles adjacent to the indent's edges in the non–cross-linked nanocomposite (Fig. 2A), probably occurred upon the tip retraction due to the low cohesive forces among the nanoparticles. In the cross-linked case, this phenomenon is not present, and the material seems to accommodate the indenter's tip without yielding to almost any lateral damage. Cracking starts occurring at increasing indentation depths (consistently from a 700-nm depth for Berkovich tip; see fig. S3). AFM topography data add information in the third dimension, perpendicular to the plane of the image, and reveal the presence of pile-ups around indents in both materials, even if much more marked in the non–cross-linked nanocomposite (Fig. 2, B, C, F, and G). We attribute this effect to the higher organic content and weaker interparticle interactions in the non–cross-linked material, as detailed in the following. Pile-up phenomena also become more significant at higher indentation depths (for both non–cross-linked and cross-linked materials; fig. S4).

By comparing the volumes of the pile-ups and the indented volumes (Berkovich) at the different indentation depths, we see that when cross-linking is absent, pile-ups occupy ~35 to 75% of the indented volume, while only ~10 to 35% in the cross-linked material. The ratio increases with increasing indentation depth. Note that this estimation does not include the effect of potential viscous deformations and time-dependent recovery, meaning that the ratios could be partially underestimated (see text S3 and table S1) and that in regions of elevated stress concentrations, such as the indent's tip, cracking may occur. Even in these cases, however, the detected volumes hint at two distinct phenomena for how the nanocomposites accommodate the displacement imposed by the indenting tip. When the organic phase is not cross-linked, the nanoparticles

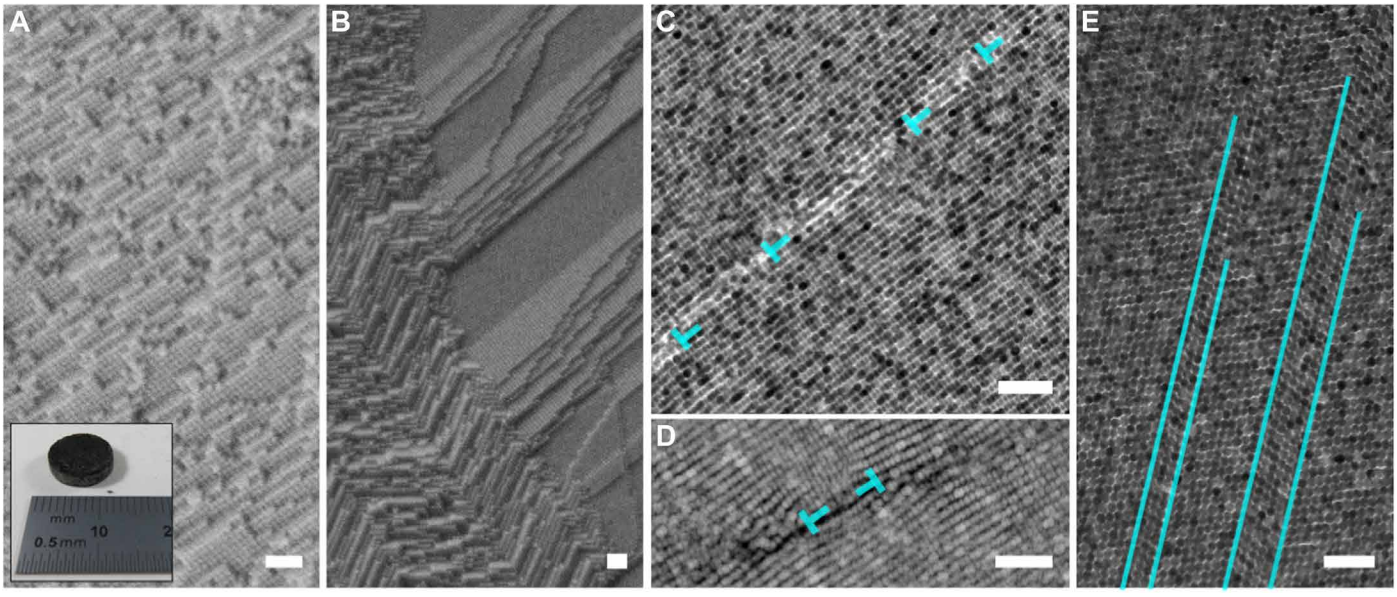

Fig. 1. Nanostructure and defects in iron oxide–oleic acid bulk supercrystalline nanocomposites. (**A**) Single supercrystal FCC nanostructure and bulk pellet after processing. Photo credit: Diletta Giuntini, Hamburg University of Technology. (**B**) Intersupercrystalline interface (high-angle grain boundary). (**C**) Low-angle grain boundary. (**D**) Frank partial. (**E**) Twins. (A) and (B) are SEM micrographs, (C) and (E) are TEM micrographs, and (D) is a STEM high-angle annular dark field micrograph. The FCC superlattice is visualized along the [11$\bar{2}$] projection axis in (C) and (D), while along the [10$\bar{1}$] axis in (E). Scale bars, 100 nm. The defects depicted here are detected regardless of cross-linking.

are only held together by weak (i.e., van der Waals) interactions and can thus easily rearrange around the tip. After cross-linking, the covalent bonds do not allow such a facile material rearrangement, and thus, compaction under the indenting tip likely becomes significant. Compaction can occur by further interdigitation and bending of the organic molecules at the nanoparticles' interfaces, as well as consequent reduction of the interparticle distances (*9*), and additionally thanks to the tetrahedral and octahedral interstitial sites characteristic of FCC lattices. On the basis of the SAXS and thermogravimetric analysis (TGA) data, it is estimated that the interstitial sites are empty in the cross-linked material, while they contain ~7 volume % of organic phase in the non–cross-linked case (see text S4 and fig. S5). Both nanocomposites have, therefore, room for compaction, even if the non–cross-linked material has a small portion of its interstitial sites filled with organic molecules that are unbound to the nanoparticles surface and possibly also with residuals of solvent trapped during the self-assembly process. This difference (7 volume %) is, however, not sufficient to explain the very distinct pile-up extents in the two materials (Fig. 2, C and G), and we thus identify the nanoparticles' interactions as the controlling parameter in how the nanocomposites accommodate indentation.

Without cross-linking, nanoparticle rearrangement plays a major role. Once a covalent network of cross-linked ligands is present to hold the nanoparticles together, rearrangement is hindered, and compaction, or more in general redistribution of the organic ligands, prevails. This is then considered as a deformation mechanism additional to subindent dislocation-mediated plasticity, as TEM observations will confirm, and a distinguishing feature of supercrystalline nanocomposites with respect to atomic crystals, enabled by the presence of an oligomeric interphase. Note also that, although compaction can have an influence on the mechanical properties measured via nanoindentation, this deformation mechanism is part of the intrinsic material response to loading and should not be disregarded. To measure elastic modulus and hardness, an appropriate indentation depth has to be large enough to sample a representative volume for a material with a superlattice length scale of ~10 nm but still avoid inducing severe damage and alterations. A depth of 300 nm is chosen, and microcompression and microbending tests result in mechanical properties that agree with nanoindentation data (*7*).

Finite element (FE) simulations supported these observations. By homogenizing the FCC superlattice into a macroscopic continuum, the nanocomposites' plastic deformation due to indentation was captured. This homogenization allows treating the material as macroscopically isotropic, which is a suitable description for the quasi-isotropic FCC superstructure in the complex multiaxial loading state introduced by the nanoindenter's tip (*2*). Inputs to the simulations were the nanocomposites' compressive strength (1.1 GPa) and the assumption of elastic-perfectly plastic constitutive behavior for the organic phase and linear elastic behavior for the inorganic nanoparticles, resulting in an elastic-perfectly plastic response of the overall nanocomposites. All details on the numerical implementation are given in (*35*) and summarized in Materials and Methods, text S5, and figs. S6 and S7. A very good matching is reached between nanoindentation experiments and simulations relative to Berkovich tip, in terms of force-displacement curves and pile-ups phenomena. Figure 2I shows pile-ups around the indent after withdrawal of the Berkovich tip in the cross-linked material (500-nm indentation depth), while Fig. 2J shows the sink in in the complementary plot. The height of the pile-ups matches well with experimental data (~15 to 25 nm according to AFM), and excellent agreement is also found for the 300-nm indentation depth (figs. S4 and S7, A to C). Figure 2K shows the resulting plastic zone (see Materials and Methods for strains calculation). Note that both AFM and FE method (FEM) outcomes are relative to the stage posterior to tip retraction and

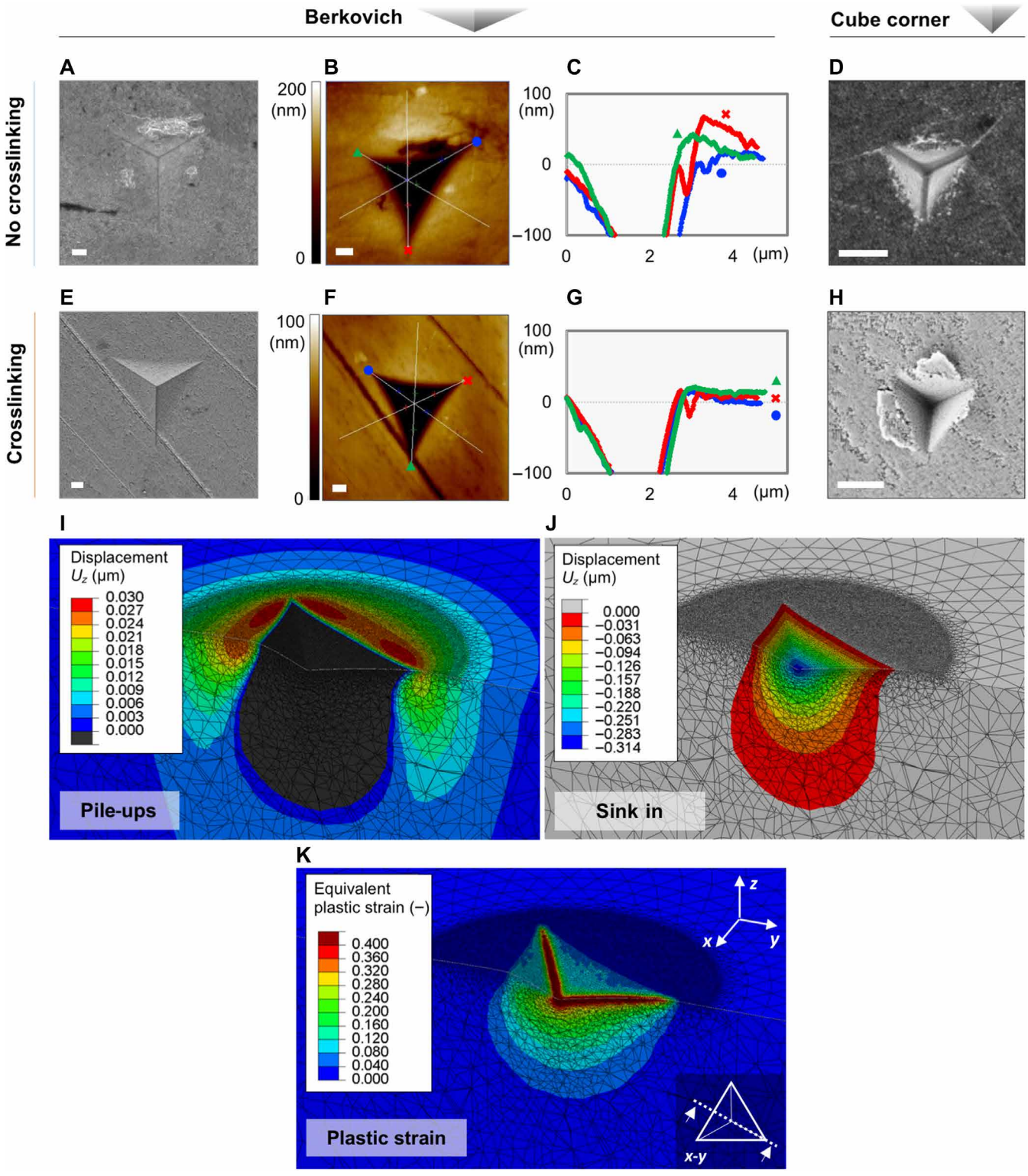

Fig. 2. Nanoindentation of supercrystalline nanocomposites. (**A** to **D**) Indents in the non–cross-linked supercrystalline nanocomposites. (A) SEM micrograph of a 500-nm-deep Berkovich indent. (B and C) AFM topography map and profiles of the indent shown in (A). (D) SEM micrograph of a 300-nm-deep cube-corner indent [reproduced with permission from (*7*)]. (**E** to **H**) Indents in the cross-linked supercrystalline nanocomposites. (E) SEM micrograph of a 500-nm-deep Berkovich indent. (F and G) AFM topography map and profiles of the indent shown in (E). (H) SEM micrograph of a 300-nm-deep cube-corner indent. Scale bars, 500 nm. (**I** to **K**) Pile-ups (I), sink-in (J), and equivalent plastic strain (K) resulting from FE simulations of a Berkovich indentation, 500 nm in depth, in the cross-linked material. The visualized subindent cross section is marked in the inset of (K). In (I), the pile-ups are highlighted by only plotting material displacements above the surface, in direction perpendicular to it (*z*); in (J), the complementary plot is shown.

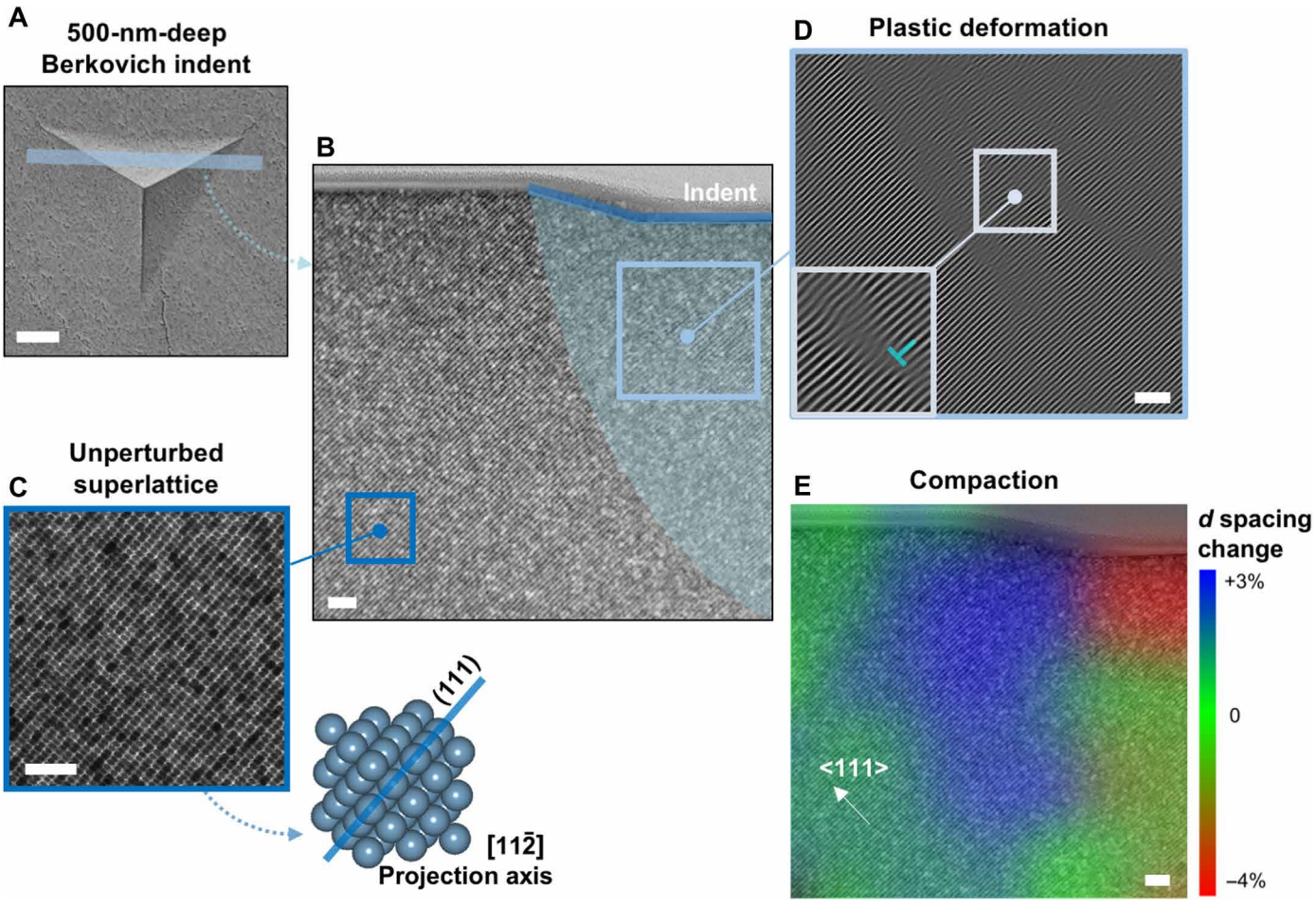

Fig. 3. Deformation under indent in supercrystal with cross-linking of the organic ligands. (**A**) Indent's area from which the lamella was extracted. (**B**) TEM image of half the lamella, with highlight of the deformed subindent area. (**C**) Higher-resolution TEM micrograph of the unperturbed superlattice away from the indent, with the respective FCC unit cell orientation. (**D**) Plastically deformed area under the indent, with highlighted (111) planes, revealing dislocation-like structures arranged along concentric arrays. (**E**) Map of the alterations in the spacing among (111) planes, *d*, with respect to the equilibrium value (14.1 nm), revealing compression and expansion zones in the superlattice. The indent is of the Berkovich type, 500 nm in depth. Scale bars, 500 nm (A) and 100 nm (B) to (E).

thus to elastic recovery, but the FEM framework does not include viscous phenomena (object of ongoing work). In the cube-corner indents (Fig. 2, D and H), the higher stress concentration induced by the more acute face angle (see Materials and Methods) leads to damage already at the shallowest indentation depths (300 nm in the figure) in the form of cracking and chipping in the non–cross-linked and cross-linked materials, respectively. Because the FE simulations did not include damage phenomena, the good agreement with experimental data found for the Berkovich tip was not obtained for the cube corner (figs. S6 and S7, E and F).

Plasticity in subindents areas

Both experimental observations of pile-up phenomena and FE outcomes point at the presence of plastic deformation as a result of nanoindentation in the supercrystalline nanocomposites. To visualize this at the superlattice scale, we visualized thin FIB lamellae (five to six layers of nanoparticles in thickness) in the TEM. Figure 3 shows the area below a 500-nm-deep Berkovich indent in the cross-linked material. A representative portion of the indented area is shown (Fig. 3, A and B), but analogous deformation patterns were identified also in the adjacent zone and under additional indents in the same material (text S6 and fig. S8). Away from the indent (Fig. 3C), the unperturbed superlattice can be observed, with tightly packed (111) planes imaged along the [11$\bar{2}$] projection axis. Below the indent, an area with perturbed superlattice is highlighted. By filtering an inset of the micrograph in that deformed area (Fig. 3D), in a way such that the (111) planes are highlighted, arrays of edge dislocation-like features are observable, distributed concentrically below the indent (see fig. S11). Such a plastic zone is very reminiscent of the ones observed below indents in single crystals (*36*). Even the shape, extended further in depth with respect to the classic model of Nix and Gao (*37*), corresponds to what has been observed during in situ TEM indentation of defect-free FCC crystalline domains with uniform orientation (*38*). The dislocation density, ρ, in the plastically deformed area appears to be lower than in typical atomic crystals. At the same time, however, the Burgers vector's modulus of supercrystalline dislocations is two orders of magnitude larger than in atomic crystals—tens of nanometers instead of angstrom. The total strain energy associated with presence of dislocations is the product of the dislocation energy per unit length ($\sim Gb^2/2$, with G as the

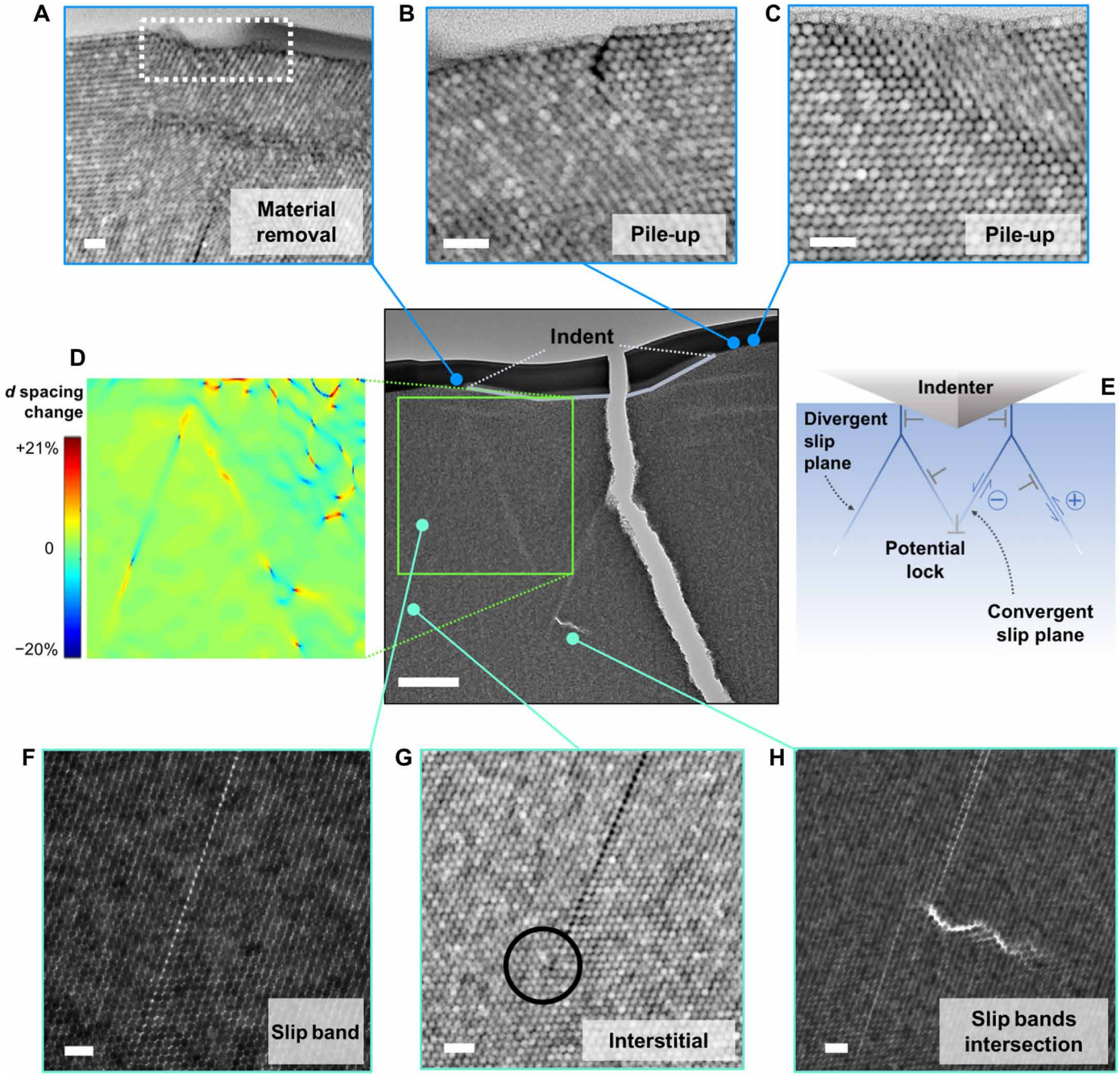

Fig. 4. Deformation under indent in supercrystal without cross-linking of the organic ligands. (**A**) Surface material removal. (**B** and **C**) Pile-ups around the indent's edges. (**D**) Mapping of the interplanar spacing changes among tightly packed {111} planes, *d*, with respect to the equilibrium value (14.8 nm). Planes of the {111} family oriented almost horizontally with respect to the applied load were selected for the mapping. (**E**) Scheme of slip bands and dislocation movement in analogy with shear patterns observed under indents in atomic single crystals (*41*, *42*). Tension and compression areas are also marked, with positive and negative sign, respectively. Note the matching of these patterns in (D) and (E). (**F** to **H**) Slip bands features, in the central area of an external slip band (F), at the termination of the same external slip band, where an interstitial is detected (G), and at the intersection between two internal bands, where cleavage is detected (H). The indent is of the Berkovich type, 500 nm in depth. Scale bars, 500 nm (central reference image) and 50 nm (all other micrographs).

shear modulus and *b* as the Burgers vector's modulus) and ρ (*39*). Atomic crystals have typically dislocation energies of ~10^{-9} J/m, while the supercrystals considered here reach ~10^{-6} J/m. Up to supercrystalline dislocation densities that are three orders of magnitude lower than in atomic crystals, then the overall strain energy stays comparable in the two cases.

Compaction, and more in general rearrangement of the organic interphase's distribution, is also confirmed to be occurring as a reaction

to indentation in cross-linked supercrystalline nanocomposites, a phenomenon that is typically detected in nanolaminates, instead of in atomic single crystals (*36*). Figure 3E shows a map of the change in spacing (d) among tightly packed (111) planes with respect to the equilibrium value (based on SAXS data, $d = a/\sqrt{3} = 14.1$ nm). Compaction up to 4% is detected immediately under the indent, while superlattice expansion up to 3% appears moving toward the edges of the indent. This is likely associated with a redistribution of the organic phase, and the compaction/expansion distribution pattern is analogous to what detected by molecular dynamics simulations for plastic deformation and pile-ups formation under indents in FCC crystals (*40*). Note that the lamella was obtained relatively close to the edge of the indent (Fig. 3A) but 15- to 25-nm-high pile-ups are present around these indents (fig. S4).

In this cross-linked material, with an initial interparticle distance of 1.5 nm, there is room for material compaction via additional confinement of the organic ligands. An increase in inter-(111) planes distance of 3%, in turn, corresponds to an increase in interparticle distance up to 2 nm. Because the oleic acid molecule can reach ~2 nm at full extension and we assume cross-linking to mainly occur at the double bond site at the center of the molecule (*2*), such a superlattice expansion is still compatible with the preservation of the covalent bonds' network. More severe shifts in the supercrystalline lattice could, instead, lead to breakage of these bonds [likely at the weaker carboxylate-Fe bond at the inorganic-organic interface (*2*)] and the consequent damage accumulation and cracking (*7*), differently from what occurs in metallic crystals. Even in such a case, however, the option of reintroducing these bonds can be explored.

When organic cross-linking is not present, the shear deformations induced by indentation become more severe. Figure 4 shows the subindent area relative to a 500-nm-deep Berkovich indent in the non–cross-linked nanocomposite. The lamella unfortunately broke during handling, but the various features are still clearly observable. At the surface of the lamella, one can observe the facile material rearrangement characterizing the non–cross-linked supercrystals, in the form of surface material removal (one to three layers of functionalized nanoparticles; Fig. 4A) and pile-ups (Fig. 4, B and C), sometimes affected by cracking. The slip band patterns induced via indentation fit extremely well with the observations and models of Keh (*41*) and Le Bourhis and co-workers (*42*) on Vickers indents in single crystals, as Fig. 4 (D and E) highlights. After a short vertical shear deformation pattern (parallel to the indentation load and typically uninfluenced by the local crystallographic orientation), the generated dislocations split into two with $\frac{a}{2}$<110> Burgers vector and start gliding on {111} planes, along both divergent (external) and convergent (internal) slip planes. These kinds of shear band configurations have been detected in crystals with lower ductility and fracture toughness compared to metallic crystals, such as the supercrystalline nanocomposites studied here are (*7*). Note also that, although dislocation dissociation into partials is energetically favorable, it is not unambiguously identified in the current investigation, suggesting that the length scale of the interparticle interaction is not yet clear.

Figure 4D shows a map of the spacing variations among {111} planes (d) with respect to the equilibrium value, 14.8 nm (in agreement with SAXS). The planes oriented almost horizontal to the loading axis were selected as most indicative of the material's tension or compression. The superlattice spacing changes (up to 20%) are significantly more severe than in the cross-linked case. At the same indentation depth, therefore, the absence of covalent bonds among neighboring organic ligands allows reaching larger interparticle distances with respect to the heat-treated material. This does not change the nature of the interactions holding the material together, but it is reasonable to consider that higher distances among the nanobuilding blocks imply weaker attractive forces among them along the slip bands. If we assume that the main attractive interaction between nanoparticles are of the London–van der Waals type, given the ratio between interparticle distance (here $ID = 2.4$ nm before deformation) and the nanoparticle radius ($R = 7.9$ nm), then we can estimate the attractive force as $F = \frac{A}{48R}\left(\frac{2R}{ID}\right)^2$, where A is the Hamaker constant (estimated as 30 to 400 zJ for iron oxide particles interfaced by hydrocarbons) (*43*, *44*). The most widespread increase in interplanar spacing d is ~5%, and this results in a ~50% decrease in F. The most severe deformations, a 20% lattice expansion, lead instead to attractive interactions that are 15% of the predeformation state. Note that lattice compression patterns are also present. The mapping reveals a complex deformation gradient across the indented area, with compression-dominated region right below the indent- and shear-dominated region in its vicinity. In the former, short-range compression-extension patterns indicative of dislocations also appear (analogously to the cross-linked material), while alternating compression-extension patterns are observed along the slip bands, due to the different shear directions. The distribution of compression and extension areas along convergent and divergent slip planes, respectively, corresponds to the models proposed for atomic crystals (see Fig. 4, D and E) (*41*, *42*). Figure 4F shows a magnified image of one such slip band, while Fig. 4 (G and H) shows slip bands' terminations in the form of an interstitial nanoparticle and cleavage. The latter likely results from a lock at the intersection of two convergent slip planes (*45*).

These slip bands were not observed in the cross-linked material at the same indentation depth, thanks to its higher resistance to deformation. To achieve the same 500 nm in depth, we applied a load of 3.5 mN here, while we needed 18 mN in the cross-linked material (see text S7 and fig. S9 for nanoindentation curves). The non–cross-linked material also shows nonlinearities in the loading curve, likely associated with the formation of the slip bands shown in Fig. 4, and a more marked tendency to creep, currently under investigation. To feature these kinds of slip bands, nanoparticles' sliding steps need to be larger than the displacements that stretched cross-linked molecules allow before breaking. This can also be rationalized in terms of Peierls potential. Without organic cross-linking, the interactions holding the nanoparticles together are weaker, and therefore, the Peierls potential is lower, leading to lower strength and higher dislocation densities. Once cross-linking is present, the limited extendibility of the covalently bonded ligands greatly hampers large shear deformation. It is also worth mentioning explicitly here that the physicochemical mechanisms leading to the formation of cross-links are still being studied and that a better understanding of the organic molecules' configuration will shed light on how much plasticity cross-linked supercrystals can ultimately accommodate.

Shear strength analysis

To understand which mechanisms control the detected shear at the superlattice scale, we applied the continuum theories of the shear behavior of crystalline materials (*39*, *45*). Two models are considered and compared to experimental data: the theoretical shear strength model, which is applicable if the superlattice is assumed to be defect-free, and the Peierls-Nabarro stress, which here would be

representative of the superlattice friction against movement of a dislocation along its slip system. For an FCC deforming along its preferential slip system ({111} <110>), the theoretical shear strength is typically estimated as to lie in the interval $\tau_{th} \in [G/5.1, G/30]$, with G as the shear modulus of the material (*45*). The Peierls-Nabarro stress is, instead, expressed as $\tau_{PN} = G \cdot \exp(-2\pi W/b)$, with W and b as the dislocation width and Burgers vector modulus, respectively. The dislocation width is given as $W = d/(1 - \nu)$, with ν as the Poisson's ratio of the nanocomposites (0.34, from the same FE simulations) (*35*, *45*). The superlattice and dislocation data (d as the interplanar spacing and b as the Burgers vector) are calculated on the basis of the SAXS-obtained lattice parameters –a = 25.7 nm and a = 24.5 nm. The shear modulus is obtained on the basis of the nanoindentation data as $G = E/[2(1 + \nu)]$, resulting in G = 6.9 GPa for the non–cross-linked material and G = 22.8 GPa for the cross-linked one. We then obtain $\tau_{th} \in [0.2, 1.4]$ GPa for non–cross-linked nanocomposites and $\tau_{th} \in [0.8, 4.5]$ GPa for the organically cross-linked case. The Peierls-Nabarro stress, instead, becomes τ_{PN} = 4.7 and 15.5 MPa. These values can then be compared to the measured strength of the nanocomposites as resulting from compression of micropillars, assuming that failure by shear is governing the response of these structures. The measured strength values are τ_C = 0.3 GPa (non–cross-linked material) and τ_C = 1.1 GPa (cross-linked) (*2*). These values correspond to ~G/20 for both types of materials, which are in the range of τ_{th}, and additionally agree with the model of Gilman for homogeneous dislocation nucleation (*46*), therefore suggesting that the supercrystalline materials probed here have an extremely low number of preexisting defects. It should also be mentioned that two lamellae were analyzed per material type (cross-linked or not) and very similar nanoindentation data were obtained in both cases. The measured values of elastic modulus and hardness, via nanoindentation with a Berkovich tip on the areas analyzed in the lamellae, show a remarkable repeatability. The two lamellae in the non–cross-linked material resulted to have E = 18.7 and 18.5 GPa and H = 0.69 and 0.75 GPa, while the heat-treated ones had E = 60.5 and 61.6 GPa and H = 4.10 and 4.27 GPa. These discrepancies within the same type of material are much lower than the scatter that is well known to affect supercrystalline nanocomposites and, thus, hint at defects being responsible for such a scatter (*2*, *7*).

The mechanical properties reported above are thus among the highest achievable in supercrystalline nanocomposites consisting of ~16-nm spherical nanoparticles functionalized with a monolayer of cross-linked molecules of oleic acid. A further enhancement would rely on altering the inorganic nanoparticles size and shape, for a maximization of the strong ceramic phase and tighter packing, and in shifting to a ligand with higher binding energy to the nanoparticles or with the option of developing more cross-links. An analysis of the inorganic nanoparticles' size effect on the overall material's behavior, in connection with existing studies on colloidal crystals, would also be of interest. Increasing the nanocomposites' ductility, on the other hand, can rely on alterations of the organic phase by the introduction of additional tailored ligand molecules, which would also enable altering the material's compaction behavior. Although the ability of these nanocomposites (ultrastrong for these inorganic-organic materials) to deform plastically is itself remarkable, their van der Waals or covalent interactions do not allow as much plastic deformation before fracture as in presence of metallic bonds. Supercrystalline inorganic-organic nanocomposite materials with these high mechanical properties and the ability to deform plastically can find applications as biomimetic structural materials and bioimplants (*47*) and as robust components for batteries and sensors.

MATERIALS AND METHODS

Samples composition and processing

The oleic acid–functionalized iron oxide (Fe_3O_4) nanoparticles are initially suspended in toluene [Center for Applied Nanotechnology (CAN)–Fraunhofer Institut für Angewandte Polymerforschung (Applied Polymer Research Institute) (IAP), Germany]. The formation of the supercrystalline structure is induced via self-assembly by solvent destabilization with ethanol as destabilizing agent, directly in a die/punch assembly. The die diameter is 14 mm. The self-assembly process lasts 15 days. The obtained supercrystalline material is dried under vacuum and then pressed in a rigid die at 150°C, leading to nanocomposites in the form of bulk cylindrical pellets, 14 mm in diameter and 4 mm in thickness. Each resulting pellet is poly-supercrystalline and contains ~7.5 weight % (wt %) of oleic acid. The organic ligands' cross-linking can then be induced by heat treatment at 325°C for 18 min, with 1°C/min heating and cooling ramps, in nitrogen atmosphere. The final organic content is ~3.5 wt %. The oleic acid content has been determined via TGA in a Mettler Toledo TGA/DSC1 STARe System, by heating the initial suspension from 25° to 900°C with a 1°C/min rate in nitrogen gas atmosphere (820 ml/min flow) (see fig. S5).

Small-angle x-ray scattering

SAXS was conducted at the High Energy Materials Science (P07) beamline, operated by Helmholtz-Zentrum Geesthacht at the PETRA III storage ring at the Deutsches Elektronen-Synchrotron (*48*). The energy of the incident beam was 87.1 keV (wavelength, 0.01423 nm), and the cross section was 0.2 mm by 0.2 mm. A 2D Perkin-Elmer detector (200-μm pixel size) was placed at a sample-to-detector distance of 3402 mm to detect the scattering signal. FIT2D was used for the data reduction (*49*). For the calculation of the particle sizes and the determination of the supercrystalline lattice parameters, the software Scatter was used (*50*), assuming a hard sphere model and a Schulz-Zimm size distribution of the particle radius and a number density-based fitting. We assume that, because of their size distribution, the nanoparticles with the most frequent radius form the supercrystals (while outliers lead do mainly amorphous areas), so the value corresponding to the maximum of the size distribution was considered most representative (7.9 nm), instead of the mean radius (8.1 nm).

Nanoindentation

Indents with increasing penetration depths (300, 500, and 700 nm, 15 indents per depth) were performed after polishing the samples' surfaces with media of decreasing roughness, from SiC papers down to a 50-nm diamond suspension. The indentation method was continuum stiffness measurement, performed with Berkovich and cube-corner tips (Synton-MDP Ltd., Switzerland) in an Agilent Nano Indenter G200 (Agilent, USA). The face angle of the Berkovich tip is 65.27°, while the cube-corner one is 35.26°. Because of the higher stress concentration induced by the more acute cube-corner tip, the elastic (Young's) modulus and hardness values reported are the ones measured with the conventional Berkovich tip (*7*).

SEM, FIB, TEM, and AFM

Portions of poly-supercrystalline pellets were cut with a diamond saw and fixed on SEM holders with silver glue (Acheson Silver DAG

1415M) in a way such that the cross section could be observed. The cross-section surface was investigated with a Zeiss SUPRA 55-VP SEM (Zeiss, Germany) and with a FEI Helios G3 UC SEM/FIB (FEI, USA) at 1 to 2 kV, both in secondary electrons (SE) mode. A FIB lamella for TEM investigation was prepared using the same FEI Helios system, by depositing a 20 µm by 2 µm protective layer of platinum on the indent and extracting the lamella using a standard lift-out procedure onto a Cu lift-out grid. The final thickness of the lamella is estimated to be 100 nm. TEM and STEM imaging was performed on a FEI Talos F200X (Thermo Fisher Scientific, USA) operating at 200 kV. STEM images are acquired with a beam current of 50 pA. Image analysis of TEM micrographs and creation of Bragg-filtered images and displacement maps were performed with the software package Fiji/ImageJ. The {111} lattice spacing map of Fig. 4 is performed using a MATLAB toolbox, CrysTBox (*51*). The image is manually calibrated by Fourier transforming the original image and matching the {111} reflection with the spacing that was measured by SAXS (14.8 nm here). The accuracy of the calibration is also confirmed by the real space (bright-field) imaging. Topography measurements were conducted via AFM (AFM NanoScope IV, Dimension 3100 of Digital Instruments), 1-Hz scan speed.

FE simulations

Multiscale FE simulations were implemented to reproduce the heat-treated (325°C), i.e., cross-linked, material's response to nanoindentation. The numerical model setup is described elsewhere (*35*) and, here, summarized for the reader's convenience. The FCC superlattice is described with the corresponding array of iron oxide nanoparticles, covered by a thin shell representative of the soft oleic acid layer, with empty interstitial sites. The FE simulations proceed to a homogenization of the unit cell into a macroscopic continuum. The experimentally measured compressive strength of the nanocomposites is given as input. The ceramic nanoparticles and the organic phase/agents are considered linear elastic (Young's modulus, $E = 163$ GPa; Poisson's ratio, $\nu = 0.3$) and elastic-perfectly plastic, respectively. Thus, the overall homogenized nanocomposite is elastic-perfectly plastic as well. The organic phase is considered as a solid, due to its high confinement, anchoring to the nanoparticles surfaces and covalently cross-linked state. A Drucker-Prager model without work hardening is selected to capture the elastoplastic behavior of both organic phase and overall nanocomposites. The nanocomposite is also assumed to be compressible ($\nu = 0.3$). Once matching of experimental and numerical nanoindentation curves is achieved, the model is considered validated. The mechanical properties of the organic phase are then derived, as $E = 13$ GPa and $\nu = 0.495$, and the nanocomposites' Poisson's ratio is recalculated, as $\nu = 0.34$. In the nanoindentation simulations, the indenting tips (Berkovich and cube corner) have $E = 1140$ GPa and $\nu = 0.07$. In these simulations, superlattice parameter and nanoparticle size were chosen as representative of a broader set of samples and, thus, differ slightly from the ones measured for the samples analyzed here via AFM and TEM (a superlattice constant of 26 nm and a nanoparticle radius of 8.8 nm). We assume that the deformation mechanisms induced by indentation are unchanged. The equivalent plastic strain is expressed as $\bar{\varepsilon}^{pl} = \int c^{-1}\,\sigma{:}\mathrm{d}\varepsilon^{pl}$, with c cohesion (parameter for Drucker-Prager yield function), σ stress tensor, and ε^{pl} plastic strain tensor.

SUPPLEMENTARY MATERIALS

Supplementary material for this article is available at http://advances.sciencemag.org/cgi/content/full/7/2/eabb6063/DC1

REFERENCES AND NOTES

1. M. R. Begley, D. S. Gianola, T. R. Ray, Bridging functional nanocomposites to robust macroscale devices. *Science* **364**, eaav4299 (2019).
2. A. Dreyer, A. Feld, A. Kornowski, E. D. Yilmaz, H. Noei, A. Meyer, T. Krekeler, C. Jiao, A. Stierle, V. Abetz, H. Weller, G. A. Schneider, Organically linked iron oxide nanoparticle supercrystals with exceptional isotropic mechanical properties. *Nat. Mater.* **15**, 522–528 (2016).
3. E. Sturm, H. Cölfen, Mesocrystals: Past, present, future. *Crystals* **7**, 207 (2017).
4. M. P. Pileni, Supra- and nanocrystallinity: Specific properties related to crystal growth mechanisms and nanocrystallinity. *Acc. Chem. Res.* **45**, 1965–1972 (2012).
5. M. A. Boles, M. Engel, D. V. Talapin, Self-assembly of colloidal nanocrystals: From intricate structures to functional materials. *Chem. Rev.* **116**, 11220–11289 (2016).
6. B. Domènech, M. Kampferbeck, E. Larsson, T. Krekeler, B. Bor, D. Giuntini, M. Blankenburg, M. Ritter, M. Müller, T. Vossmeyer, H. Weller, G. A. Schneider, Hierarchical supercrystalline nanocomposites through the self-assembly of organically-modified ceramic nanoparticles. *Sci. Rep.* **9**, 3435 (2019).
7. B. Bor, D. Giuntini, B. Domènech, M. V. Swain, G. A. Schneider, Nanoindentation-based study of the mechanical behavior of bulk supercrystalline ceramic-organic nanocomposites. *J. Eur. Ceram. Soc.* **39**, 3247–3256 (2019).
8. D. Giuntini, E. Torresani, K. T. Chan, M. Blankenburg, L. Saviot, B. Bor, B. Domènech, M. Shachar, M. Müller, E. A. Olevsky, J. E. Garay, G. A. Schneider, Iron oxide-based nanostructured ceramics with tailored magnetic and mechanical properties: Development of mechanically robust, bulk superparamagnetic materials. *Nanoscale Adv.* **1**, 3139–3150 (2019).
9. B. Domènech, A. Plunkett, M. Kampferbeck, M. Blankenburg, B. Bor, D. Giuntini, T. Krekeler, M. Wagstaffe, H. Noei, A. Stierle, M. Ritter, M. Müller, T. Vossmeyer, H. Weller, G. A. Schneider, Modulating the mechanical properties of supercrystalline nanocomposite materials via solvent–ligand interactions. *Langmuir* **35**, 13893–13903 (2019).
10. A. S. Baimuratov, I. D. Rukhlenko, V. K. Turkov, A. V. Baranov, A. V. Fedorov, Quantum-dot supercrystals for future nanophotonics. *Sci. Rep.* **3**, 1727 (2013).
11. S. C. Glotzer, M. J. Solomon, Anisotropy of building blocks and their assembly into complex structures. *Nat. Mater.* **6**, 557–562 (2007).
12. M. P. Pileni, Nanocrystal self-assemblies: Fabrication and collective properties. *J. Phys. Chem. B* **105**, 3358–3371 (2001).
13. T. Tachikawa, T. Majima, Metal oxide mesocrystals with tailored structures and properties for energy conversion and storage applications. *NPG Asia Mater.* **6**, e100 (2014).
14. D. V. Talapin, J.-S. Lee, M. V. Kovalenko, E. V. Shevchenko, Prospects of colloidal nanocrystals for electronic and optoelectronic applications. *Chem. Rev.* **110**, 389–458 (2010).
15. E. Tam, P. Podsiadlo, E. Shevchenko, D. F. Ogletree, M.-P. Delplancke-Ogletree, P. D. Ashby, Mechanical properties of face-centered cubic supercrystals of nanocrystals. *Nano Lett.* **10**, 2363–2367 (2010).
16. P. Podsiadlo, G. Krylova, B. Lee, K. Critchley, D. V. Talapin, P. D. Ashby, E. V. Shevchenko, The role of order, nanocrystal size, and capping ligands in the collective mechanical response of three-dimensional nanocrystal solids. *J. Am. Chem. Soc.* **132**, 8953–8960 (2010).
17. X. W. Gu, Mechanical properties of architected nanomaterials made from organic–inorganic nanocrystals. *JOM* **70**, 2205–2217 (2018).
18. M.-P. Pileni, Mechanical properties of supracrystals. *Europhys. Lett.* **119**, 37002 (2017).
19. K. E. Mueggenburg, X.-M. Lin, R. H. Goldsmith, H. M. Jaeger, Elastic membranes of close-packed nanoparticle arrays. *Nat. Mater.* **6**, 656–660 (2007).
20. A. T. L. Tan, J. Beroz, M. Kolle, A. J. Hart, Direct-write freeform colloidal assembly. *Adv. Mater.* **30**, e1803620 (2018).
21. N. Goubet, M. P. Pileni, Analogy between atoms in a nanocrystal and nanocrystals in a supracrystal: Is it real or just a highly probable speculation? *J. Phys. Chem. Lett.* **2**, 1024–1031 (2011).
22. N. Goubet, J. Richardi, P.-A. Albouy, M.-P. Pileni, Which forces control supracrystal nucleation in organic media? *Adv. Funct. Mater.* **21**, 2693–2704 (2011).
23. M. I. Bodnarchuk, E. V. Shevchenko, D. V. Talapin, Structural defects in periodic and quasicrystalline binary nanocrystal superlattices. *J. Am. Chem. Soc.* **133**, 20837–20849 (2011).
24. P. Schall, I. Cohen, D. A. Weitz, F. Spaepen, Visualization of dislocation dynamics in colloidal crystals. *Science* **305**, 1944–1948 (2004).
25. H. Hwang, D. A. Weitz, F. Spaepen, Direct observation of crystallization and melting with colloids. *Proc. Natl. Acad. Sci. U.S.A.* **116**, 1180–1184 (2019).
26. A. V. Zozulya, J.-M. Meijer, A. Shabalin, A. Ricci, F. Westermeier, R. P. Kurta, U. Lorenz, A. Singer, O. Yefanov, A. V. Petukhov, M. Sprung, I. A. Vartanyants, In situ x-ray crystallographic study of the structural evolution of colloidal crystals upon heating. *J. Appl. Cryst.* **46**, 903–907 (2013).

27. K. E. Jensen, D. Pennachio, D. Recht, D. A. Weitz, F. Spaepen, Rapid growth of large, defect-free colloidal crystals. *Soft Matter* **9**, 320–328 (2013).
28. W. T. M. Irvine, A. D. Hollingsworth, D. G. Grier, P. M. Chaikin, Dislocation reactions, grain boundaries, and irreversibility in two-dimensional lattices using topological tweezers. *Proc. Natl. Acad. Sci. U.S.A.* **110**, 15544–15548 (2013).
29. F. A. Lavergne, A. Curran, D. G. A. L. Aarts, R. P. A. Dullens, Dislocation-controlled formation and kinetics of grain boundary loops in two-dimensional crystals. *Proc. Natl. Acad. Sci. U.S.A.* **115**, 6922–6927 (2018).
30. P. Schall, I. Cohen, D. A. Weitz, F. Spaepen, Visualizing dislocation nucleation by indenting colloidal crystals. *Nature* **440**, 319–323 (2006).
31. S. Suresh, Colloid model for atoms. *Nat. Mater.* **5**, 253–254 (2006).
32. F. Gallego-Gómez, V. Morales-Flórez, Á. Blanco, N. de La Rosa-Fox, C. López, Water-dependent micromechanical and rheological properties of silica colloidal crystals studied by nanoindentation. *Nano Lett.* **12**, 4920–4924 (2012).
33. M. Roth, C. Schilde, P. Lellig, A. Kwade, G. K. Auernhammer, Simultaneous nanoindentation and 3D imaging on semicrystalline colloidal films. *Chem. Lett.* **41**, 1110–1112 (2012).
34. Materials and methods are available as supplementary materials.
35. M. Li, I. Scheider, B. Bor, B. Domènech, G. A. Schneider, D. Giuntini, Ultra-thin and ultra-strong organic interphase in nanocomposites with supercrystalline particle arrangement: Mechanical behavior identification via multiscale numerical modeling. *Compos. Sci. Technol.* **198**, 108283 (2020).
36. S. Lloyd, A. Castellero, F. Giuliani, Y. Long, K. McLaughlin, J. Molina-Aldareguia, N. Stelmashenko, L. Vandeperre, W. Clegg, Observations of nanoindents via cross-sectional transmission electron microscopy: A survey of deformation mechanisms. *Proc. R. Soc. A* **461**, 2521–2543 (2005).
37. W. D. Nix, H. Gao, Indentation size effects in crystalline materials: A law for strain gradient plasticity. *J. Mech. Phys. Solids* **46**, 411–425 (1998).
38. A. M. Minor, E. T. Lilleodden, E. A. Stach, J. W. Morris, Direct observations of incipient plasticity during nanoindentation of Al. *J. Mater. Res.* **19**, 176–182 (2004).
39. M. A. Meyers, K. K. Chawla, *Mechanical Behavior of Materials* (Cambridge Univ. Press, ed. 2, 2009).
40. J. Varillas, J. Očenášek, J. Torner, J. Alcalá, Unraveling deformation mechanisms around FCC and BCC nanocontacts through slip trace and pileup topography analyses. *Acta Mater.* **125**, 431–441 (2017).
41. A. S. Keh, Dislocations in indented magnesium oxide crystals. *J. Appl. Phys.* **31**, 1538–1545 (1960).
42. E. Le Bourhis, J. P. Riviere, A. Zozime, Material flow under an indentor in indium phosphide. *J. Mater. Sci.* **31**, 6571–6576 (1996).
43. H. C. Hamaker, The London—van der Waals attraction between spherical particles. *Phys. Ther.* **4**, 1058–1072 (1937).
44. B. Faure, G. Salazar-Alvarez, L. Bergström, Hamaker constants of iron oxide nanoparticles. *Langmuir* **27**, 8659–8664 (2011).
45. J. P. Hirth, J. Lothe, *Theory of Dislocations* (McGraw-Hill, 1968).
46. J. J. Gilman, Dislocation sources in crystals. *J. Appl. Phys.* **30**, 1584–1594 (1959).
47. M. Eder, S. Amini, P. Fratzl, Biological composites–complex structures for functional diversity. *Science* **362**, 543–547 (2018).
48. N. Schell, A. King, F. Beckmann, T. Fischer, M. Müller, A. Schreyer, The High Energy Materials Science Beamline (HEMS) at PETRA III. *MSF* **772**, 57–61 (2013).
49. A. P. Hammersley, *FIT2D: An Introduction and Overview*, (Internal Report ESRF97HA02T, ESRF, 1997).
50. S. Förster, L. Apostol, W. Bras, *Scatter*: Software for the analysis of nano- and mesoscale small-angle scattering. *J. Appl. Cryst.* **43**, 639–646 (2010).
51. M. Klinger, More features, more tools, more *CrysTBox*. *J. Appl. Cryst.* **50**, 1226–1234 (2017).

Acknowledgments: We acknowledge W. Kaplan and E. Lilleodden for the valuable support and insightful discussions. **Funding:** We acknowledge financial support from the Deutsche Forschungsgemeinschaft (DFG, German Research Foundation), project number 192346071-SFB 986. D.G. acknowledges the support from the Alexander von Humboldt Foundation. B.B. acknowledges the support from the Ministry of National Education of the Republic of Turkey. **Author contributions:** D.G. designed the study, conducted the experimental and theoretical modeling work, and wrote the manuscript. S.Z. conducted the image analysis and collaborated to the mechanical behavior study. T.K., G.S., and M.R. collaborated to and supervised the electron microscopy work and the subsequent image analysis. M.L. and I.S. conducted the numerical simulations. M.B. and M.M. conducted and supervised the SAXS analysis. B.B. and B.D. conducted the sample preparation and contributed to the material characterization. G.A.S. supervised the work. All authors contributed to the manuscript writing. **Competing interests:** The authors declare that they have no competing interests. **Data and materials availability:** All data needed to evaluate the conclusions in the paper are present in the paper and/or the Supplementary Materials. Additional data related to this paper may be requested from the authors.

Submitted 6 March 2020
Accepted 19 November 2020
Published 8 January 2021
10.1126/sciadv.abb6063

Citation: D. Giuntini, S. Zhao, T. Krekeler, M. Li, M. Blankenburg, B. Bor, G. Schaan, B. Domènech, M. Müller, I. Scheider, M. Ritter, G. A. Schneider, Defects and plasticity in ultrastrong supercrystalline nanocomposites. *Sci. Adv.* **7**, eabb6063 (2021).

Defects and plasticity in ultrastrong supercrystalline nanocomposites

D. Giuntini, S. Zhao, T. Krekeler, M. Li, M. Blankenburg, B. Bor, G. Schaan, B. Domènech, M. Müller, I. Scheider, M. Ritter and G. A. Schneider

Sci Adv **7** (2), eabb6063.
DOI: 10.1126/sciadv.abb6063